RESEARCH ARTICLE

BIOPHYSICS

Alcanivorax borkumensis biofilms enhance oil degradation by interfacial tubulation

M. Prasad[1]†, N. Obana[2,3], S.-Z. Lin[4], S. Zhao[1], K. Sakai[5,6], C. Blanch-Mercader[7],
J. Prost[7,8], N. Nomura[1,3,9], J.-F. Rupprecht[4]*, J. Fattaccioli[5,6]*, A. S. Utada[1,3]*

During the consumption of alkanes, *Alcanivorax borkumensis* will form a biofilm around an oil droplet, but the role this plays during degradation remains unclear. We identified a shift in biofilm morphology that depends on adaptation to oil consumption: Longer exposure leads to the appearance of dendritic biofilms optimized for oil consumption effected through tubulation of the interface. In situ microfluidic tracking enabled us to correlate tubulation to localized defects in the interfacial cell ordering. We demonstrate control over droplet deformation by using confinement to position defects, inducing dimpling in the droplets. We developed a model that elucidates biofilm morphology, linking tubulation to decreased interfacial tension and increased cell hydrophobicity.

Obligately hydrocarbonoclastic bacteria (OHCB) are a group of cosmopolitan marine bacteria with an unusual ecology: They can survive by consuming hydrocarbons as a sole carbon and energy source (*1*). These metabolic specialists are found at very low densities because of the lack of hydrocarbons but are thought to play a global role in metabolizing naturally occurring alkanes (*2*) in the ocean. However, they become the dominant bacteria, out-competing generalists, at the site of oil spills (*1*, *3*, *4*). OHCB are thought to degrade a substantial fraction of spilled oil worldwide (*1*, *5*), which has generated interest for their potential as agents of bioremediation (*5–9*).

Alcanivorax borkumensis SK2 is an aerobic and rod-shaped OHCB (*10*) that is often used as a model organism for prevalence (*1*, *2*) and its genetic tractability (*6*, *11*). Like most bacteria, it transitions between planktonic and biofilm lifestyles, which is now recognized as integral to bacterial biology (*12*). Biofilms are often dense three-dimensional communities encased in self-secreted extracellular polymeric substances, which adhere them to surfaces. Biofilms begin with the colonization of a surface. This can lead to high two-dimensional cell densities, which in the case of rod-shaped bacteria, induces nematic liquid crystal order. Bacteria have been shown to escape confinement in dense packings (*13*, *14*) by leveraging regions where the nematic order is undefined, called topological defects (*15*). Unlike most bacteria, because *A. borkumensis* forms biofilms on a liquid, it is not clear how the interfacial fluidity affects cell packing and biofilm morphology formation during oil consumption.

Most knowledge of bacteria-mediated oil degradation comes from chemical, genetic, and metagenomic analysis of ocean samples (*7*, *16*, *17*) and microcosm tests that used crude oil and sea water (*18–20*). Recent work has begun to clarify the important initial step of bacterial colonization (*21*) and to characterize biofilm formation (*22–25*) on oil drops in the size range commonly found dispersed in the ocean after an oil spill. Biofilms can deform oil drops (*18*, *24*, *25*) and increase their hydrodynamic drag (*23*), potentially mediating the formation of organic-oil aggregates. These aggregates, also known as marine oil snow, have been identified as a mechanism by which large quantities of partially biodegraded oil was transported to the seafloor in the aftermath of the Deepwater Horizon disaster (*4*, *23*, *26*). However, the mechanism of biofilm formation, which depends on the interfacial properties of individual cells, and its relation to oil degradation remains unclear (*18*).

Experimental setup and microfluidic device

To address these questions, we developed a microfluidic device that allows the trapping and real-time imaging of numerous bacteria-covered oil droplets. This platform allows us to capture the full dynamics of biofilm development starting from individual bacteria through the complete consumption of oil droplets.

In the ocean, *A. borkumensis* subsists primarily on naturally occurring organic acids and alkanes (*2*); however, during oil spills, it blooms to exploit the hydrocarbons in the crude oil mélange. To study the biofilm dynamics as *A. borkumensis* adapts (*27*) to using solely alkanes, we initially cultivated using pyruvate and then switched to an artificial seawater medium supplemented with hexadecane (C16) (fig. S1A). We sampled bacteria from liquid cultures cultivated up to 5 days by harvesting the cells and generating cell-laden oil microdroplets with fresh C16, which we incubated in individual microfluidic traps (supplementary text S1). Our device, which is highly permeable to oxygen, facilitates in situ culturing, enabling the longitudinal investigation of biofilm development simultaneously on numerous droplets (Fig. 1A and fig. S2A). Trapped drops initially had approximately 20 to 50 cells attached and reached confluency in ~12 hours, which we define as t_0 (fig. S3A).

Bacteria exhibit two distinct phenotypes and consumption rates

Testing different liquid cultures at 1 and 5 days revealed different phenotypes that manifested vastly different biofilm morphologies and oil consumption rates. When sampled after 1 day, *A. borkumensis* formed a spherical biofilm (SB) that grew outward from the oil, and the oil droplet remained mostly spherical as it was consumed (Fig. 1B, fig. S3B, and movie S1). By contrast, bacteria sampled from 5-day-old culture can develop into thin biofilms with a local nematic ordering of the interfacial cells, which eventually buckle and then tubulate (*24*, *25*) the droplet interface (Fig. 1C), which we call dendritic biofilms (DB) (supplementary text S2). The biofilm buckles the interface to accommodate a population that is continuously increasing in number. The magnitude of the deformations grows as the oil is consumed, which ultimately shreds the droplets into tiny fragments (fig. S3C and movie S2).

To quantify the oil consumption rate for each phenotype, we measured the oil volume (*V*) over time using confocal microscopy. SBs consumed >90% of their oil droplet volume in ~72 hours, whereas DBs achieved the same level of consumption in ~20 hours. We found that the oil volume of SBs decreases as a polynomial function of time, whereas for DBs, the decay is much faster (Fig. 1, D and E, and fig. S3, D to F). In both cases, the decrease is consistent with a model of oil consumption effected exclusively by bacteria at the interface (supplementary text S3).

The good agreement between our analytical models and data allows us to estimate the single-cell consumption rates of oil by the SB and

[1]Faculty of Life and Environmental Sciences, University of Tsukuba, Tsukuba, Ibaraki 305-8577, Japan. [2]Transborder Medical Research Center, Faculty of Medicine, University of Tsukuba, Tsukuba, Ibaraki 305-8577, Japan. [3]Microbiology Research Center for Sustainability (MiCS), University of Tsukuba, Tsukuba, Ibaraki 305-8577, Japan. [4]Aix Marseille Univ, Université de Toulon, CNRS, CPT (UMR 7332), Turing Centre for Living systems, Marseille, France. [5]PASTEUR, Département de Chimie, École Normale Supérieure, PSL Université, Sorbonne Université, CNRS, 75005 Paris, France. [6]Institut Pierre-Gilles de Gennes pour la Microfluidique, 75005 Paris, France. [7]Laboratoire Physico-Chimie Curie UMR168, Institut Curie, Paris Sciences et Lettres, Centre National de la Recherche Scientifique, Sorbonne Université, 75248 Paris, France. [8]Mechanobiology Institute, National University of Singapore, 117411 Singapore. [9]TARA center, Univeristy of Tsukuba, Tsukuba, Ibaraki 305-8577, Japan.
*Corresponding author. Email: utada.andrew.gm@u.tsukuba.ac.jp (A.S.U.); jacques.fattaccioli@ens.psl.eu (J.F.); jean-francois.rupprecht@univ-amu.fr (J.-F.R.)
†Present address: School of Biosciences, University of Sheffield, Sheffield, UK.

Fig. 1. Spherical and dendritic biofilm phenotypes on oil drops in a microfluidic trap. (**A**) (Left) Schematic of the microfluidic oil-drop trap device, showing media-filled channels. Oil drops are trapped in the raised circular regions. Inlets on either side of the drop chamber connect to reservoirs that provide a gentle flow of media through the trap chamber. The white circles indicate pillars. Scale bar, 200 μm. (Middle) Schematic cross-section of an individual trap. (Right) Bright-field image of a representative drop in a trap. The trap is outlined with a white dashed line, and the pocket is colored orange as a guide for the eye. Scale bar, 20 μm. (**B**) Representative time-lapse sequence of confocal images showing the development of the SB phenotype. As the biofilm (green) grows, the oil droplet (central void) shrinks. Scale bar, 10 μm. (**C**) Maximum intensity projection confocal images showing the development of the DB phenotype on representative drops. Local nematic order is present at confluence (~0 hours), buckling (0.1 to 0.5 hours) and protrusions (2 to 4 hours) appear later, and large-scale remodeling of the interface leading to the formation of tubes occurs much later (16 hours). Scale bar, 10 μm. (**D** and **E**) Normalized surface area (S^*) and volume (V^*) of oil drops as a function of time for (open circles) SBs and (stars) DBs. Solid lines and shaded regions indicate mean ± SD (n_{SB} = 11 drops, and n_{DB} = 12 drops; representative experiment from three or more independent tests) (additional data is provided in fig. S3). Solid symbols indicate measurements, and open symbols indicate values calculated from measured quantities. The dashed and dotted lines are best fits of our analytical models of oil degradation for the phenotypes. [(D), inset] Normalized drop radius (R^*) was used to estimate S^* and V^* for SBs. [(E), inset] S^*/V^* as a function of time. R, S, and V are normalized by their initial values, respectively. We used eqs. S5, S6, S9, and S11 (supplementary text S3) to fit R^*, S^*, and V^* for SB and DBs, respectively.
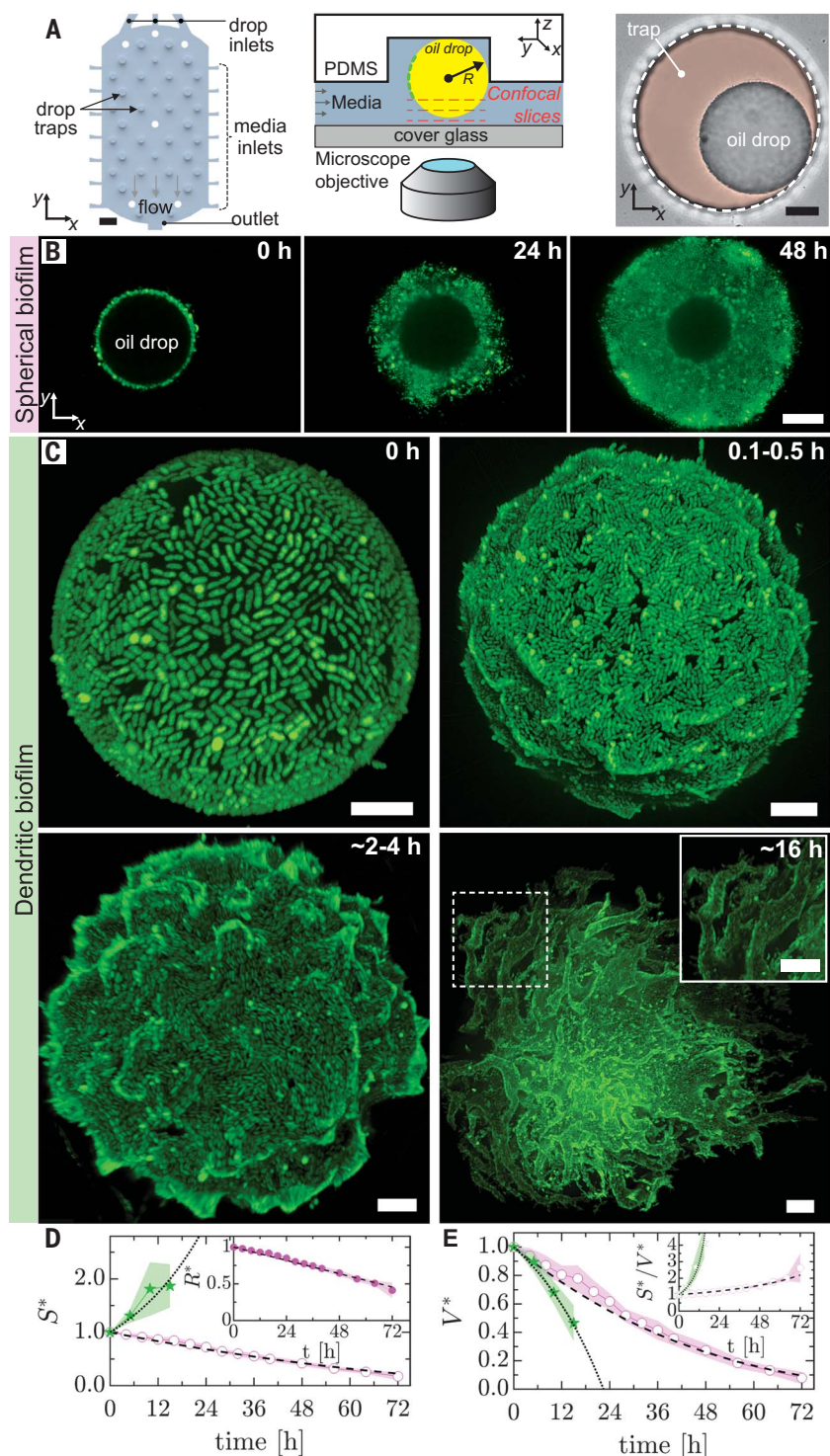
DB cells as 0.7 and 0.8 fl/hour, respectively. This small difference in consumption rate is consistent with their similar division times (fig. S1D). For comparison, the volume of a single cell is ~1 fl, meaning that these bacteria consume a volume of oil close to their own, every hour. Despite the similarity in consumption rates on a per-cell basis, the normalized surface-to-volume ratio (S^*/V^*) shows that DBs are considerably more efficient: S^*/V^* doubles in 72 hours for SBs, whereas it diverges in less than 24 hours for DBs (Fig. 1E, inset). The S^*/V^* ratio provides a means for comparing the relative efficiencies of the two phenotypes and highlights that these differences arise from the rapid increase in interfacial area caused by DB biofilms. In both cases, the shape of the interface defines the dynamics of volume decrease. For SBs, the interfacial area defined by the spherical droplet determines the number of cells (N) that can pack onto the interface to have access to the oil. Conversely, for DBs, it is the increase of N at the interface due to cell division that determines the interfacial area. Thus, the rate of consumption decreases over time for SBs, whereas it increases continuously for DBs.

Tubulation is facilitated by topological defects

We correlated the onset of the rapid increase in surface area for DBs to the emergence of nematic order of the interfacial cells. Active systems with nematic order have shown the ability to use topological defects to achieve surface deformation, both theoretically (28, 29) and experimentally (supplementary text S4) (13, 14, 30). Nematic topological defects of charge ±1/2 and ±1 are shown schematically in fig. S4A. At 2 to 4 hours after confluency, we observed the appearance of conical protrusions of cells that originate from the core of aster (+1) topological defects in the nematic director field, which is the average orientation of the bacteria (Fig. 2, A and B; fig. S4B; and supplementary text S3). As the biofilm matures, more protrusions appear, while existing protrusions elongate into branched bacteria-covered tubes (Figs. 1C, 16 hours, and 2C).

Differential labeling of the oil and cells shows that the tubes are not filled with water; instead, they are filled with oil (fig. S5A). This indicates that cell adhesion to the oil stabilizes the tubes against collapse, preventing the deformed oil from regaining a spherical shape. Furthermore, careful inspection of the confocal images of the tubes reveals that the bacteria are well aligned to the tube axis, which becomes clear in the director field of the cells on the tube (Fig. 2D). We characterized cell alignment along the tube with the local average scalar product between the director field and the tube axis, finding values close to 1; this indicates a high degree of alignment between the cells and the tube axis (Fig. 2E and fig. S5, B and C).

Because of this alignment, we hypothesized that the rate of increase of the tube length is proportional to the number of cells on the tube, which should increase exponentially if all cells were to divide. We measured tube elongation on different droplets and found that it increases rapidly and in a manner consistent with exponential elongation, which supports this hypothesis (Fig. 2F and fig. S5D). Furthermore, from the fit to our data, we extracted a tube length–doubling time of ~3.4 hours, which is twofold greater than the cell division time (t_{div}) of 1.65 hours (fig. S1D). This difference likely arises from the imperfect alignment of cells along the tubes and the expulsion of cells from the interface, which is visible around the tubes (Fig. 2C).

Biofilm phenotypes are associated with a decrease of interfacial tension

The large difference in biofilm morphology between the two phenotypes suggests differences in their interfacial properties. *A. borkumensis* secretes amphiphilic molecules that are thought to aid in the assimilation of oil (10, 31–33). Furthermore, autolysis is thought to be important during *A. borkumensis* biofilm formation (11), which could liberate membrane-bound biosurfactants into the oil. These molecules can lower the oil-water interfacial tension (γ), making interfacial deformation easier. To measure changes in interfacial properties of the phenotypes, we fractionated SB and DB liquid cultures into three components—cells, conditioned media, and conditioned C16—to independently measure γ for each (fig. S6A). We found that γ for each of the respective fractions was depressed relative to control values; however, the DB-conditioned oil decreased the most. The γ for DB-conditioned oil decreased from 32 to 7 mN/m and was about half the value for SBs (Fig. 3A; fig. S6, B to D; and table S1). Unexpectedly, when we microfluidically tested SB and DB cells using the DB-conditioned C16 instead of fresh C16, we found no change in observed phenotype (fig. S6E). Thus, despite the ~80% lower γ of DB-conditioned oil, the SB cells were unable to deform the oil-water interface, indicating that a lower γ is not sufficient to produce the DB phenotype.

Interfacial behavior is also affected by cell hydrophobicity, which together with γ controls the extent that oil wets the cells (fig. S7A). Cell hydrophobicity is thought to increase the longer that cells consume oil, potentially through accumulation of membrane-bound hydrophobic
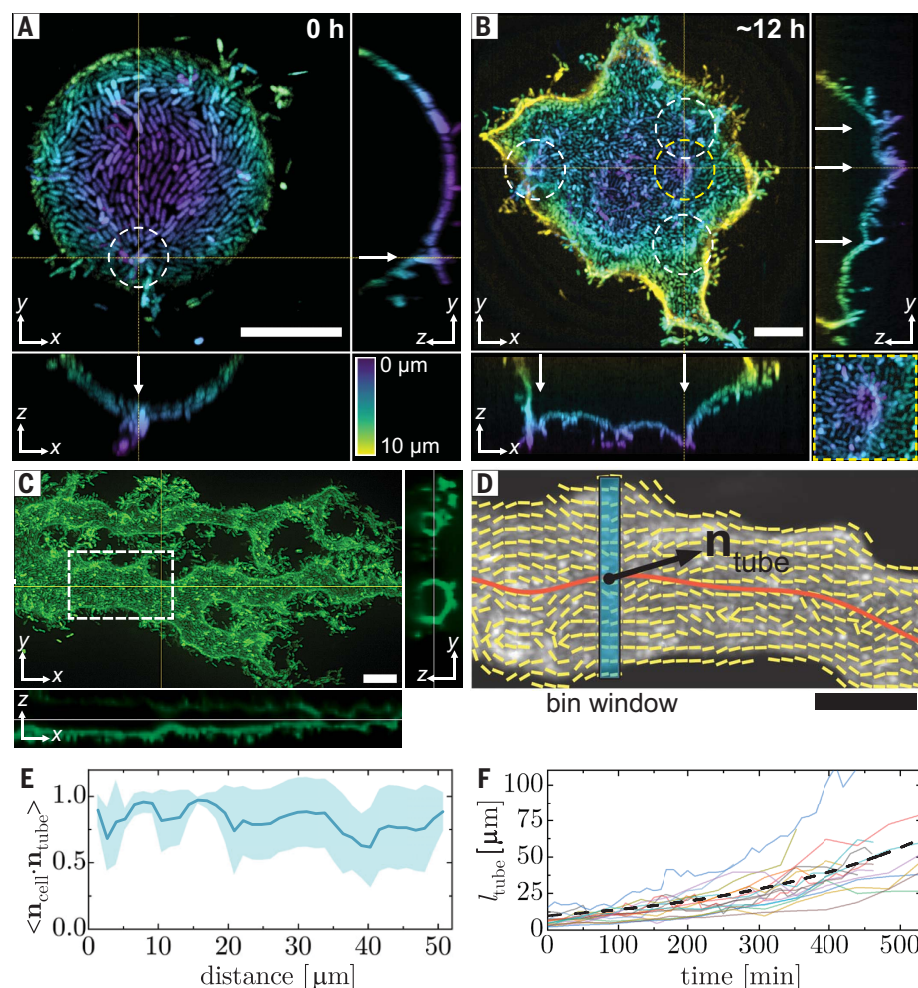

Fig. 2. Dendrites originate from topological defects. (**A** and **B**) Confocal images of representative droplets (A) early (~0 hours) and (B) later (~12 hours) in biofilm development. The images are color coded by depth. The dashed circles enclose +1 topological defects, and the arrows indicate protrusions. [(B), inset] Magnified view of the central defect circled in yellow. (**C**) Confocal image of a bacteria-covered tube connected to a deformed droplet with corresponding orthogonal views (~20 hours). (**D**) Director field of the visible cells in the dashed box in (C). The director field (yellow lines), tube axis (red line), the local tangent unit vector ($\mathbf{n}_{tube}$) along the tube axis, and the bin window (blue) are shown. (**E**) Axial order of the cells along the oil tube shown in (D). For a sliding window of width 1.5 μm along the tube, the local axial order is defined as the average of the individual scalar products between the director-field unit vectors ($\mathbf{n}_{cell}$) and local tangent unit vectors. $\langle \mathbf{n}_{cell} \cdot \mathbf{n}_{tube} \rangle = 1$ for parallel alignment and 0 for perpendicular alignment. Solid line and shaded region are mean ± SD. (**F**) Oil tube length (l_{tube}) plotted as a function of time (n = 18 tubes; three independent tests). The dashed line is a fit to the average tube length from using an exponential equation [adjusted coefficient of determination (R^2) = 0.96]. Scale bars, 10 μm.

biosurfactants (*33*); however, the relationship with phenotype is unclear (*19, 34*). Although the bacteria appear to lay flat on the surface at t_0, the contact angle is difficult to estimate from confocal images (fig. S7B). Thus, to estimate cell hydrophobicity of both phenotypes, we measured the three-phase contact angle (θ) between a water drop deposited on a bacterial lawn submerged in oil (fig. S7, C to E) (*35*); larger θ values indicate greater hydrophobicity. SB cells, which were isolated after 1 day of culture, had a θ ≈ 80°, whereas DB cells, which were isolated after 5 days, had a θ ≈ 100° (Fig. 3B). This suggests that the midplanes of SB and DB cells were ±10% above and below the interface, respectively (fig. S7A).

The higher hydrophobicity of DB cells also indicates that they have a larger interfacial adhesion strength than that of SB cells, for a constant γ (supplementary text S4). To directly compare the respective adhesion strengths of SB and DB, we forced them to compete for interfacial area on oil microdroplets, noting that both phenotypes have similar division times (fig. S1D). We generated cell-laden droplets using mCherry-expressing SB cells and green fluorescent protein (GFP)–expressing DB cells in a 3:1 ratio and recorded fluorescence intensity as the biofilm developed. In this test, both phenotypes experienced the same γ. We found that although the DB cells were initially in the minority, they dislodged the established SB, becoming dominant in ~5 hours (Fig. 3, C and D). This confirmed our expectation that DB cells, which are more hydrophobic, do indeed have a larger adhesion energy to the interface than that of SB cells.

Rod-shaped gammaproteobacteria such as *Pseudomonas aeruginosa* have been shown to colonize and remodel oil-water interfaces with their biofilms, similar to what we observed in the early stages (<3 hours) of DB formation (*36, 37*). However, those biofilms lack the large-scale deformations produced by DBs (Fig. 1C, >5 hours). Using our γ, we estimated the biofilm compression modulus to be ~200 Pa (*38*), which is much smaller than the ~1 MPa growth pressure of *P. aeruginosa* (*39*). Assuming a similar growth pressure for *A. borkumensis*, cell division supplies enough stress to easily deform the interface. Thus, DBs generate the biofilm phenotypes we observed only if enough cells remain adhered to the interface to drive the tubulation process. Conversely, the lack of deformations in the SB phenotype is the consequence of insufficient cell hydrophobicity combined with a stiffer interface, leading to cell detachment followed by biofilm formation around the droplet.

Membrane theory predicts the transition from SB to DB phenotype

On the basis of these observations, we developed a coarse-grain membrane model to describe the interfacial dynamics of the growing
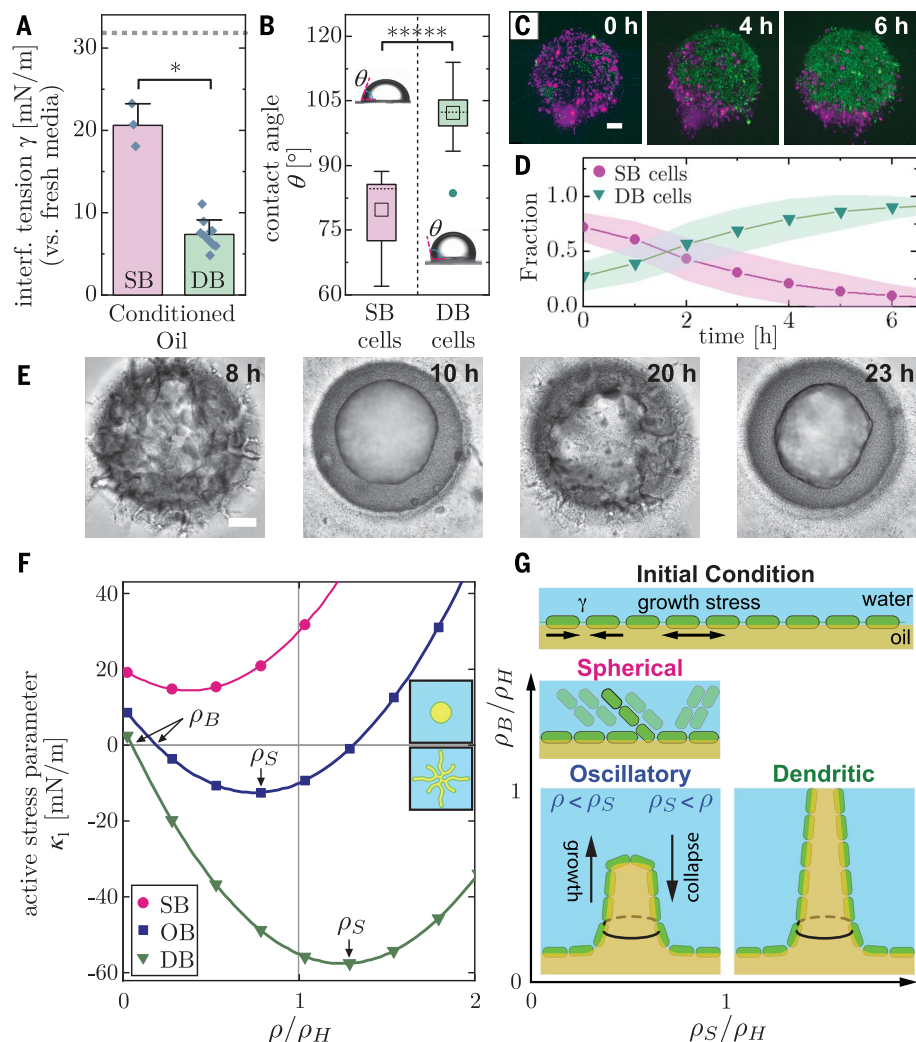

Fig. 3. Theoretical model of tubulation. (**A**) Interfacial tension (γ) between biofilm-conditioned oil and fresh media measured with pendant drop tensiometry for SBs and DBs, respectively. The dashed line indicates γ between fresh oil and fresh medium [mean + SD; n_{SB} = 3, n_{DB} = 10, $n_{control}$ = 5 independent tests; *P < 0.05 (P = 0.012), Welch's t test with Holm-Bonferroni correction]. (**B**) Three-phase contact angle (θ) between a water drop deposited on a bacterial lawn of SB and DB phenotypes, submerged in oil. Open squares indicate mean; horizontal dashed lines indicate medians; and the solid circle indicates an outlier [n_{SB} = 10, n_{DB} = 13 independent tests; *****P < 0.00001 (P = 1.2 × 10^{-6}), Welch's t test]. (Inset) Images of water drops on bacterial lawns, submerged in oil. (**C**) Time-lapse sequence of the competition between SB cells (magenta) and DB cells (green) for interfacial area on a trapped droplet. Droplets are generated in a suspension containing SB and DB cells at a ratio of 3:1 (supplementary text). DB cells displace a monolayer of SB cells over the course of ~6 hours. (**D**) Measurement of the fractional coverage of SB and DB as a function of time from confocal images (solid line and filled regions indicate mean ± SD; n = 10 representative drops). (**E**) Oscillatory biofilm (OB) behavior demonstrated by a culture sampled for an intermediate duration between the SB and DB cultures. (**F**) Model of the tension (κ_1 in the phase-field model) experienced by the tip of a tube as a function of normalized interfacial cell density (ρ/ρ_H) (supplementary text). We normalized cell density by the homeostatic interfacial cell density (ρ_H). Positive and negative values of κ_1 indicate tube retraction and expansion, respectively. The slope at the y intercept is k_1 = 3, 6, and 10 for the SB, OB, and DB models, respectively. The ρ_B is the critical buckling density, where κ_1 < 0. For SBs, ρ_B = ∞. The ρ_S is the optimal cell density, where κ_1 reaches a minimum, and beyond which the effect of spontaneous curvature is reduced. (Insets) Phase-field simulation showing a circular droplet (κ_1 > 0) and a tubulated droplet (κ_1 < 0). (**G**) Schematic phase diagram of the biofilm phenotypes in terms of normalized densities: ρ_S/ρ_H and ρ_B/ρ_H. When ρ_B/ρ_H > 1, SBs form because the interfacial cell density can never become sufficiently large to induce buckling. For ρ_B/ρ_H < 1, cell division drives an increase in cell density beyond ρ_B. When ρ_S/ρ_H < 1, oscillations between the spherical and dendritic phenotypes can occur (OB). When, ρ_S/ρ_H > 1, stable dendrites (DB) occur.

interfacial biofilm. The model explains the transition between SB and DB phenotypes in terms of a competition between the interfacial tension and the spontaneous curvature of the biofilm, which is its intrinsic tendency to bend in a preferred direction. Interfacial tension resists expansion of the surface by the biofilm, whereas the spontaneous curvature of the biofilm governs the shape of the expanding surface. Tubes are generated when the energetic cost of increasing surface area is lower than the cost of bending; they expand exponentially, according to

$$\frac{\eta}{L}\frac{dL}{dt} = -\left(\sigma_{t,H} + \sigma_{n,H} - \frac{\kappa_B}{r_0 r_{eq}}\right) \quad (1)$$

where L is the tube length, η is the viscosity of the biofilm layer, $\sigma_{t,H}$ and $\sigma_{n,H}$ are the respective tensions along the circumferential and normal directions of the tube, κ_B is the bending rigidity of the membrane in the circumferential direction of the tube, $1/r_0$ is the spontaneous curvature of the biofilm, and r_{eq} is the tube radius (supplementary text S6 and fig. S14).

Equation 1 encompasses the existence of active extensile nematic stresses driven by bacterial growth, with an effective interfacial tension $\gamma_{eff}(\rho) = \frac{1}{2}(\sigma_{t,H} + \sigma_{n,H})$ that depends on the interfacial cell density (ρ) (supplementary text S6). This implies that tubulation occurs at a critical value of the buckling density (ρ_B), which is consistent with our observation that tubes form after confluency (Fig. 1C). In our model, bacteria populate a circular oil-water interface with a density that increases logistically toward a homeostatic density (ρ_H), at which division and loss are balanced. Depending on the ratio ρ_B/ρ_H, the phenotype changes: When $\rho_B/\rho_H > 1$, tubes are unable to form, resulting in the SB phenotype; when $\rho_B/\rho_H < 1$, the interface buckles and stable tubes form, producing the DB phenotype. Our model implies that physically lowering ρ by removing cells of a DB below the critical value should cause a deformed droplet to recover its unperturbed spherical shape. To test this hypothesis, we infused surfactants into a device containing DBs. We used a formulation similar to that of Corexit 9500, which is used to disperse marine oil spills, and concentrations that ranged from 25 to 100 times the critical micelle concentration (37). Our concentrations exceed estimated levels in the top 20 cm of the ocean after the Deepwater Horizon accident (4, 37). After a ~4-hour lag, the biofilm abruptly washed away, and the deformed droplets became spherical; this recovery was the consequence of positive interfacial tension in the absence of bacteria (fig. S8, A and B, and movie S3).

In addition to the SB and DB phenotypes described so far, we observed an intermediate phenotype when we isolated cells at an intermediate culture time (fig. S1A). These biofilms present dynamic oscillatory behavior (OB), alternating between the DBs and SBs, with a period of ~12 hours (Fig. 3E, fig. S9, and movie S4). The relatively short (~30 min) transition from tubulated to spherical is consistent with a sudden loss of tube stability because of a sudden increase in effective surface tension (Eq. 1).

To elucidate the emergence of oscillations between spherical and dendritic phenotypes, we used a phase-field approach following an established literature on simulating interfacial dynamics of multiphasic systems (40). In our case, the simulated field is the local fraction of oil [$\varphi(x,y)$] that obeys a Cahn-Hilliard equation with an interfacial term $\kappa_1(\rho)(\nabla\varphi)^2/2$; here, $\kappa_1(\rho)$ is defined by the right side of Eq. 1 and sets the tube elongation rate. $\kappa_1(\rho)$ is thus a proxy for the active stress along the interface (supplementary text S4). In our model, a linear relation of the form $\kappa_1(\rho) = \gamma - k_1\rho$, where k_1 accounts for the force exerted by the biofilm on the oil, is sufficient to understand the SB-to-DB transition. For the SB phenotype, the $\kappa_1(\rho)$ tension is positive for all densities, precluding tube formation. The interface remains spherical until ρ surpasses the critical density, $\rho_B = \gamma/k_1$; here, $\kappa_1(\rho)$ becomes negative, and tubulation occurs as the interface buckles. However, the morphological oscillations emerge only if we consider a second-order expansion of $\kappa_1(\rho)$ in ρ, so that an "optimal" cell density exists where tube elongation and the final tube length are maximal, which we denote ρ_S (Fig. 3F). Oscillations arise for the specific case when $\rho_B < \rho_S < \rho_H$ (supplementary text S5); here, as cell density increases beyond the optimal value ρ_S, tube elongation ceases, and contraction starts. During this contraction, the surface shrinks faster than cells can be ejected from the interface, leading to an abrupt increase in bacterial density. We found that ρ overshoots ρ_H and causes $\kappa_1(\rho)$ to become positive (Fig. 3F, blue). This dynamical overshoot ultimately induces a catastrophic collapse of the tubes and is accompanied by a large reduction in the number of cells at the interface. Consistent with this prediction, in our experiments we observed a large and persistent flow of cells away from the interface soon after tube collapse (movie S4). Our biomechanical model recapitulates the transition from these three phenotypes in terms of a tubulation mechanism that depends on bacterial growth dynamics, with oscillations emerging through a dynamical phase transition mechanism (Fig. 3G and movie S5) (41). These oscillations are driven by continuous cell division that pushes density beyond the critical values for tube growth and collapse.

Controlled buckling of confined droplets

We leveraged microfluidics to position the tube-generating topological defects through droplet confinement. By trapping droplets larger than

Fig. 4. Defect-mediated buckling of the surface of a confined droplet. (**A** to **C**) Time-lapse confocal image sequence showing the evolution of a dendritic biofilm on a "flattened" drop, color coded by depth. (A) Before confluency (−40 min), interfacial tension excludes cells from the flattened regions at the top and bottom of the droplets. These regions are generated where the nonwetting droplets contact the glass floor and polydimethylsiloxane (PDMS) ceiling. (Top inset) A droplet schematic. (Bottom inset) Top view of the droplet. (B) Confluent monolayer is formed at $t_0 = 0$ min (fig. S10). (Inset) Top view of droplet, with a circle enclosing the location of the nematic defect. (C) Dimple formation in the droplet at the defect. Scale bars, 10 μm. (**D**) Evolution of the dimple height (h) from xy-line profiles measured across the droplet midplane, at 20 min (early) and 26 ± 3 min (late) after confluency. Dimple height is shown as a function of the radial coordinate (r). The fits to the data are based on eq. S80 (supplementary text). The solid error bars and shaded regions indicate ±SD on the experimental data and fits, respectively (details on the fitting procedure and error estimation are available in the supplementary text). Early-profile data are the average of the x and y profiles ($n = 4$) at $t = 20$ min, whereas the late-profile data are the average of the x and y profiles binned at 23, 26, and 29 min ($n = 12$), respectively. To generate the dimensional values shown, we rescaled the nondimensionalized h values by the dimple heights 4.5 and 8.0 μm, at early and late times, respectively, whereas r was rescaled by 26 μm at all times.
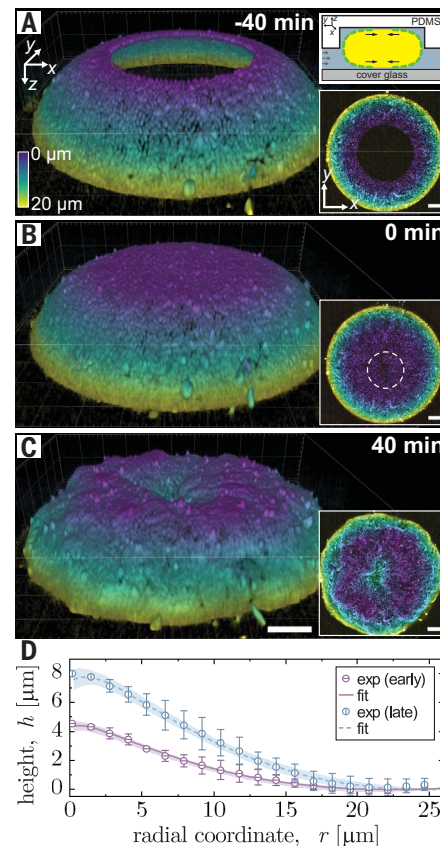
the chamber height, we can grow biofilms on flattened drops (Fig. 4A, top inset). These flat circular regions allowed us to generate a centered defect, which concentrates growth stress to form a dimple. Interfacial tension, which initially excludes bacteria from the flat region, was eventually overcome by growth pressure (Fig. 4A, fig. S10A,B, and movie S6). As cells invaded, their flow oriented the director field, which formed a single aster defect (or two narrowly separated +1/2 defects) at confluency (Fig. 4B and fig. S10, C and D) (15). As cell division continued, dimples formed at the defects at the top and bottom of the drop (Fig. 4C and fig. S10, B, inset, and E). We used the theory of liquid crystal membranes to elucidate the role of the aster defect in generating deformation in the biofilm. The dimple height profile depends on two dimensionless parameters: κ_F/κ_B, where κ_F is the elastic constant of distortions to the director field, and $\kappa_B/\gamma R_{dimple}^2$, where R_{dimple} is the radius of the dimple (supplementary text S8). κ_F/κ_B captures the competition between the elastic energy of distortions to the liquid crystalline biofilm and its bending energy, whereas $\kappa_B/\gamma R_{dimple}^2$ captures the competition between biofilm bending energy and its surface tension. Buckling at the defect occurs when the energetic cost to deform the membrane exceeds its bending energy, $\kappa_F/\kappa_B > 1$; our fits yield a ratio of ≈ 2 (fig. S11 and table S2) (29, 42). In agreement with experiments, the profiles in this parameter regime are qualitatively like pseudospheres (Fig. 4D and fig. S12) (42).

The ability of marine microorganisms to biodegrade hydrocarbons has been recognized for nearly a century (1), with recent improvements to metagenomic and imaging techniques further clarifying the possible mechanisms involved. In this study, we quantified the mechanism by which cultures of *A. borkumensis* preadapted to using an alkane leads to the appearance of a biofilm phenotype primed (43) for explosive growth. Leveraging microfluidics, we captured the dynamics of the optimized biofilms, correlating their appearance to measurable changes in the interfacial properties of the bacteria. These biofilms develop liquid crystalline order before buckling the interface at aster topological defects, morphing the spherical droplet into numerous branching dendrites. We developed a theoretical model that recapitulates each phenotype and explains the cause of the spectacular biofilm oscillations we observed. Furthermore, we used microfluidics to control the dimpling of the droplet and used the profiles to confirm the liquid crystalline elastic constant of the biofilm from theory.

Topological defects in layers of both prokaryotic and eukaryotic cells have been shown to be important in defect-driven morphogenesis (13, 14, 29, 30, 44). We found that the optimized *A. borkumensis* cells collectively use defect-driven buckling to escape the confines of the droplet interface and expand the biofilm laterally. Efficiency is achieved not through an increase of individual metabolic throughput but rather by expanding the interface, allowing more cells to simultaneously feed.

Although we found that addition of oil dispersant similar in composition to commercially available mixtures leads to the rapid detachment of the biofilm from the oil drops, numerous factors such as the dispersant concentration; oil composition, temperature, and pressure; and nutrient concentrations likely affect biodegradation. Because our platform is an open system, all inputs can be dynamically controlled; thus, how biofilm formation changes depending on hydrocarbon composition, nutrient profile, as well as the dynamical response of bacteria to dispersant dose may be independently verified. These tests could also serve as a starting point in the investigation of artificially constructed multispecies consortia (8), which are more robust and effective than monocultures (9).

REFERENCES AND NOTES

1. I. M. Head, D. M. Jones, W. F. M. Röling, *Nat. Rev. Microbiol.* **4**, 173–182 (2006).
2. C. R. Love et al., *Nat. Microbiol.* **6**, 489–498 (2021).
3. Y. Kasai et al., *Environ. Microbiol.* **4**, 141–147 (2002).
4. B. H. Gregson et al., *Front. Mar. Sci.* **8**, 619484 (2021).
5. R. M. Atlas, T. C. Hazen, *Environ. Sci. Technol.* **45**, 6709–6715 (2011).
6. S. Schneiker et al., *Nat. Biotechnol.* **24**, 997–1004 (2006).
7. T. C. Hazen et al., *Science* **330**, 204–208 (2010).
8. F. Mapelli et al., *Trends Biotechnol.* **35**, 860–870 (2017).
9. T. J. McGenity, B. D. Folwell, B. A. McKew, G. O. Sanni, *Aquat. Biosyst.* **8**, 10 (2012).
10. M. M. Yakimov et al., *Int. J. Syst. Bacteriol.* **48**, 339–348 (1998).
11. J. S. Sabirova, T. N. Chernikova, K. N. Timmis, P. N. Golyshin, *FEMS Microbiol. Lett.* **285**, 89–96 (2008).
12. L. Hall-Stoodley, J. W. Costerton, P. Stoodley, *Nat. Rev. Microbiol.* **2**, 95–108 (2004).
13. K. Copenhagen, R. Alert, N. S. Wingreen, J. W. Shaevitz, *Nat. Phys.* **17**, 211–215 (2021).
14. O. J. Meacock, A. Doostmohammadi, K. R. Foster, J. M. Yeomans, W. M. Durham, *Nat. Phys.* **17**, 205–210 (2021).
15. P. G. de Gennes, J. Prost, *The Physics Of Liquid Crystals*, International Series Of Monographs On Physics (Oxford Univ. Press, ed. 2, 1995).
16. R. M. Atlas, R. Bartha, *Biotechnol. Bioeng.* **14**, 309–318 (1972).
17. O. U. Mason et al., *ISME J.* **6**, 1715–1727 (2012).
18. R. Grimaud, in *Handbook of Hydrocarbon and Lipid Microbiology*, K. N. Timmis, Ed. (Springer Berlin Heidelberg, 2010), pp. 1491–1499.
19. M. P. Godfrin, M. Sihlabela, A. Bose, A. Tripathi, *Langmuir* **34**, 9047–9053 (2018).
20. J. Tremblay et al., *ISME J.* **11**, 2793–2808 (2017).
21. N. K. Dewangan, J. C. Conrad, *Langmuir* **34**, 14012–14021 (2018).
22. A. R. White, M. Jalali, J. Sheng, *Sci. Rep.* **9**, 13737 (2019).
23. A. R. White, M. Jalali, J. Sheng, *Front. Mar. Sci.* **7**, 294 (2020).
24. M. Omarova et al., *ACS Sustain. Chem. & Eng.* **7**, 14490–14499 (2019).
25. V. Hickl, G. Juarez, *Soft Matter* **18**, 7217–7228 (2022).
26. U. Passow, *Deep Sea Res. Part II Top. Stud. Oceanogr.* **129**, 232–240 (2016).
27. D. J. Naether et al., *Appl. Environ. Microbiol.* **79**, 4282–4293 (2013).
28. L. Metselaar, J. M. Yeomans, A. Doostmohammadi, *Phys. Rev. Lett.* **123**, 208001 (2019).
29. L. A. Hoffmann, L. N. Carenza, J. Eckert, L. Giomi, *Sci. Adv.* **8**, eabk2712 (2022).
30. P. Guillamat, C. Blanch-Mercader, G. Pernollet, K. Kruse, A. Roux, *Nat. Mater.* **21**, 588–597 (2022).
31. A. Passeri et al., *Appl. Microbiol. Biotechnol.* **37**, 281–286 (1992).
32. M. P. Kem, H. K. Zane, S. D. Springer, J. M. Gauglitz, A. Butler, *Metallomics* **6**, 1150–1155 (2014).
33. J. Cui et al., *Appl. Environ. Microbiol.* **88**, e0112622 (2022).
34. N. L. Olivera et al., *Res. Microbiol.* **160**, 19–26 (2009).
35. L. S. Dorobantu, A. K. C. Yeung, J. M. Foght, M. R. Gray, *Appl. Environ. Microbiol.* **70**, 6333–6336 (2004).
36. L. Vaccari et al., *Soft Matter* **11**, 6062–6074 (2015).
37. R. C. Prince, *Environ. Sci. Technol.* **49**, 6376–6384 (2015).
38. D. Vella, P. Aussillous, L. Mahadevan, *Europhys. Lett.* **68**, 212–218 (2004).
39. H. H. Tuson et al., *Mol. Microbiol.* **84**, 874–891 (2012).
40. J. W. Cahn, *J. Chem. Phys.* **42**, 93–99 (1965).
41. F. Jülicher, A. Ajdari, J. Prost, *Rev. Mod. Phys.* **69**, 1269–1282 (1997).
42. J. R. Frank, M. Kardar, *Phys. Rev. E Stat. Nonlin. Soft Matter Phys.* **77**, 041705 (2008).
43. D. L. Valentine et al., *Proc. Natl. Acad. Sci. U.S.A.* **109**, 20286–20291 (2012).
44. Y. Maroudas-Sacks et al., *Nat. Phys.* **17**, 251–259 (2021).
45. S.-Z. Lin, J.-F. Rupprecht, Phase-field simulation framework; model of Alcanivorax bacteria at an oil/water interface. Zenodo (2023), https://doi.org/10.5281/zenodo.8043717.

SUPPLEMENTARY MATERIALS

science.org/doi/10.1126/science.adf3345
Materials and Methods
Supplementary Text
Figs. S1 to S17
Tables S1 to S3
References (46–62)
Movies S1 to S6
MDAR Reproducibility Checklist